Rev.Adv.Mater.Sci. 18(2008) 481-493

NANOCRYSTALLIZATION IN RAPIDLY QUENCHED Fe-Mo-Cu-B: SURFACE AND VOLUME EFFECTS

Marek Paluga[1], Peter Švec[1], Dušan Janičkovič[1], Dušan Muller[1], Peter Mrafko[1] and Marcel Miglierini[2,3]

[1]Institute of Physics, Slovak Academy of Sciences, Dúbravská cesta 9, 845 11 Bratislava, Slovakia
[2]Department of Nuclear Physics and Technology, Slovak University of Technology, Ilkovičova 3, 812 19 Bratislava, Slovakia
[3] Nanomaterials Research Centre, Svobody 26, 771 46 Olomouc, Czech Republic

Received: March 29, 2008

Abstract. Transformations in rapidly quenched ribbons $Fe_{91-x}Mo_8Cu_1B_x$ for x=12-20 were investigated by diverse methods of kinetic and structure analysis. The importance of Cu as nanocrystal former was shown on the case of $Fe_{80}Mo_8B_{12}$. It was shown that a change of mechanism from a two-stage process to a single stage transformation takes place with increasing boron content. The crystallization products were identified as bcc-Fe(Mo) with the degree of supersaturation decreasing with increasing boron content, B_2Mo_2Fe, $Fe_{23}B_6$ and small amounts of Fe_3B. Special effects related to the appearance of crystalline phases at the surface layers of as-quenched ribbons were observed which contradict the usual pattern of surface crystallinity formation due to insufficient quenching rates or glass forming ability. These effects were correlated with changes of alloy composition and with addition of another element. Possible micromechanisms leading to this behavior were discussed in terms of quenched-in cluster structure.

1. INTRODUCTION

Typical transformations from rapidly quenched amorphous into nanocrystalline state usually exhibit a two-stage pattern. The first stage is represented by (nano)crystallization of metal-rich phases forming non-impinged grains of about ~10 nm in size taking up ~50% of the entire volume. This stage is followed by formation of metalloid-rich structures from the amorphous remains during the second crystallization stage, which is usually separated in temperature and time from the nanograin formation. Recrystallization into stable phases takes place at still higher temperatures.

A special case of amorphisation and nanocrystallization processes is observed in rapidly quenched Fe-Mo-Cu-B system with varying Fe to B ratio [1]. The first transformation stage is characterized for all investigated compositions by formation of ultra-fine grains of bcc-Fe well dispersed in amorphous matrix with significantly lower crystallinity content. This structure remains unchanged to temperatures well above 850K, leaving a wide temperature interval of ~100K where the nanograins and the amorphous remains coexist without noticeable coarsening of the nanocrystals.

The systems Fe-Mo-B and (Fe-Co)-Mo-Cu-B in amorphous and nanocrystalline states exhibit excellent and unique magnetic and mechanical properties. Addition of Cu as nanocrystal-refining element and partial substitution of Fe by Co lead to formation of nanostructure with different contents of very fine-grained nanocrystalline phase [2] and to possibility of tuning the Curie temperature of the system [3]. The choice of proper Fe to B ratio in

Corresponding author: P. Svec, e-mail: fyzisvec@savba.sk

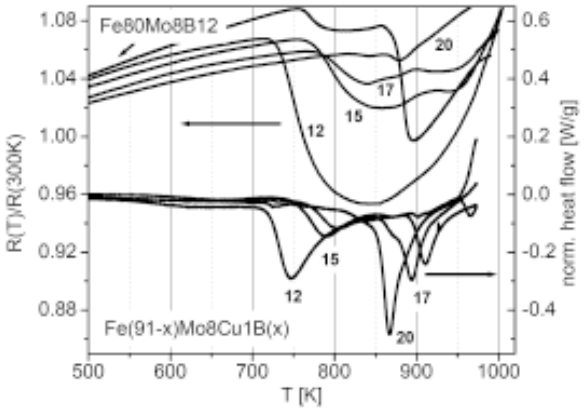

Fig. 1. Temperature dependence of relative electrical resistivity $R(T)/R(300K)$ (top) and DSC traces (bottom) of as-quenched $Fe_{91-x}Mo_8Cu_1B_x$ samples; heating rate 10 K/min. The numbers indicate boron content in at.%; resistivity curve of $Fe_{80}Mo_8B_{12}$ shown for comparison.

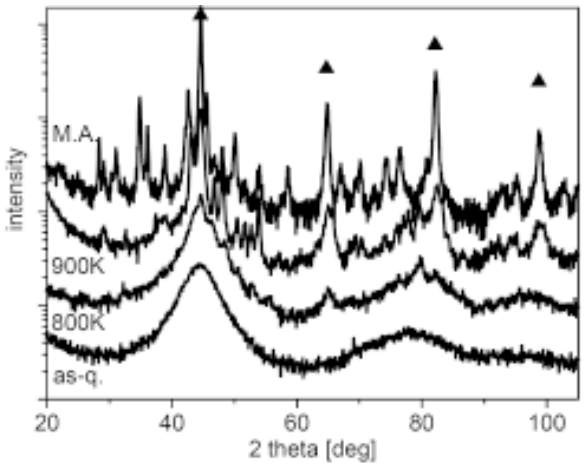

Fig. 2. X-ray patterns of $Fe_{80}Mo_8B_{12}$ in as-quenched state and after annealing at 800 and 900K for 30 min. Top curve (M.A.) – polycrystalline master alloy precursor. Solid upright triangles indicate the positions of the bcc-Fe reflections.

Fe-Mo-Cu-B system has allowed to optimise the magnitude of magnetocaloric effect in amorphous and nanocrystalline states [4] at temperatures in the vicinity of 300K, providing attractive magnetic material for the exploitation of this effect at room temperatures. A combination of ferromagnetic (Fe, Co), paramagnetic (Mo) and diamagnetic (Cu) elements has allowed the investigation of magnetomechanical effetcs (dilatation, magnetostriction) of amorphous magnetic systems in different magnetic states as a function of temperature and applied magnetic field [5]. In addition, surface properties of Fe-Mo-B systems (wear resistance) were reported to be suitable for wear-resistant layers of magnetic data carriers [6].

Special effects were observed on the surfaces of the ribbons of Fe-Mo-Cu-B in as-quenched state. The presence of anomalous quenched-in polycrystalline layers ~100 nm thick was detected at both surfaces of the otherwise fully amorphous ribbons [7]. The transformation process from as-quenched (X-ray amorphous) state in Fe-Mo-Cu-B system in the entire "volume" of the ribbons has been investigated in [8]. In this study we shall concentrate on the comparison of the structures formed both at either of the surfaces as well as in the volume of the $Fe_{91-x}Mo_8Cu_1B_x$ (x=12, 15, 17, 20) rapidly quenched ribbons, comparing also the effect of Cu addition on volume crystallization for the case of $Fe_{80}Mo_8B_{12}$. Links between the structure and atomic arrangement within the polycrystalline master alloy precursor and its melt, the expected local ordering in amorphous state and the phases formed either during rapid quenching or during its subsequent transformations are discussed in terms of the proposed melt-quenched clustered structure of the amorphous state.

2. EXPERIMENTAL

Master alloys with nominal compositions $Fe_{91-x}Mo_8Cu_1B_x$ for x=12-20 and $Fe_{80}Mo_8B_{12}$ were prepared from high-purity elements (better than 99.8%) in vacuum induction furnace. Due to the presence of refractory element with high melting point (molybdenum) the temperature of the master alloy melts was generally above 1750K, well above the estimated [9,10] and measured [1] liquidus of the alloys. In special cases, when the influence of the master alloy melt on the rapidly-quenched structure was investigated, lower (1700K) and higher (1900K) temperatures of the master alloy melt were used; master alloys of $Fe_{79}Cu_1Mo_8B_{12}$ were prepared also by arc-melting for comparison.

The as-quenched ribbons (10 mm wide, 20-22 μm thick) of nominal compositions were prepared by rapid quenching (planar flow casting) on a single copper wheel of ~500 mm diameter. In selected cases ribbons were also cast in argon-filled vacuum chamber. Standard wheel speed during planar flow casting was 35 m/sec; the $Fe_{79}Mo_8Cu_1B_{12}$ and $Fe_{74}Mo_8Cu_1B_{17}$ ribbons were prepared also at lower and higher wheel speeds, 40, 30, and 25 m/sec and with different thickness to check the effect of the quenching rate on the formation of amorphous state. Casting temperatures were selected with respect to the values of liquidus determined in the master alloys [1].

In all cases the chemical composition of the corresponding ribbons was minutely checked by emission spectrometry with inductively coupled plasma (ICP) to confirm no detectable deviation of chemical composition or presence of additional elements (Si, C, Zr, …) due to master alloy melt treatment and subsequent planar flow casting. Furthermore, the homogeneity of elemental distribution across the ribbon thickness was checked by energy-dispersive (EDX) and wavelength dispersive (WDX) analyses using a LEO 1550 scanning electron microscope (SEM); the results indicated no observable partitioning of the elements across the ribbon thickness on the scales attainable by the equipment used (~100 nm).

Pieces of ribbons ~2 cm long and 3 mm disks for TEM were isothermally annealed in high vacuum at temperatures from 330 to 750 °C for 1 hour to prepare samples with different contents of crystalline phase and to follow the different stages of the transformation process. Individual treatment temperatures were chosen according to temperature dependencies of electrical resistivity $R(T)$ measured in vacuum, which were in excellent agreement with the corresponding differential scanning calorimetry (DSC) curves measured in argon using PerkinElmer DSC 7 with the heating rate of 10 K/min [1]. The microstructure of as-quenched and nanocrystalline samples was analyzed by X-ray diffraction (XRD) with Cu*K*a radiation in Bragg-Brentano configuration with graphite monochromator in the diffracted beam and by transmission electron microscopy (TEM) and electron diffraction (ED) using JEOL 2000FX at 200 kV. Samples for TEM were polished by Ar ion beam milling in Gatan PIPS; samples were prepared in conventional way from as-quenched or thermally treated disks as well as sandwiched between Si-wafers for cross-section TEM (CS TEM) investigation.

All castings and subsequent measurements were statistically repeated and several measurement runs and analyses were performed on the same and different ribbon pieces, showing similar effects, also along the entire wheel diameter length of the ribbons.

With respect to the different surfaces of the ribbons we will use the following convention. The side of the ribbon, which was in direct contact with the quenching wheel, will be referred to as the wheel (or bottom) side. The opposite side of the ribbon, i.e. which was exposed to the surrounding atmosphere will be denoted as the air (or top) side. Bulk or volume of the thin ribbon is understood as the part of ribbon accessible after classical sample thinning evenly from both sides. Unless specified otherwise, X-ray analyses were performed with air (top) side towards the incident radiation.

3. RESULTS

3.1. Structure transformations in ribbon volume

The transformation from as-quenched state is visible by a decrease of electrical resistivity $R(T)$ or by exothermal peaks on DSC traces; for all investigated compositions the first stage of (nano)crystallization takes place above 700K (Fig. 1). Dramatic change of the character of $R(T)$ dependence due to the addition of 1 at.% of Cu can be seen from the curves corresponding to $Fe_{80}Mo_8B_{12}$ and $Fe_{79}Mo_8Cu_1B_{12}$. The first stage of crystallization of fully amorphous $Fe_{80}Mo_8B_{12}$ (above ~750K) leads to formation of supersaturated bcc-Fe(Mo) grains of ~20-30 nm embedded in amorphous matrix. The transformation of the amorphous remains takes place above 850 K, forming a mixture of tetragonal Fe_3B (I-4, no. 82), a=0.86736nm, c=0.43128 nm and tetragonal phase B_2Mo_2Fe (P4/mbm, no. 127) with parameters a=0.5775 nm, c=0.3145 nm (Figs. 2, 3). The content of the Fe_3B phase increases slightly with annealing temperature. The X-ray pattern of sample annealed above 1000K becomes identical to that of the master alloy.

The first stage of transformation in $Fe_{79}Mo_8Cu_1B_{12}$, which starts above 700K, forms truly nanocrystalline bcc-Fe(Mo) grains of ~5-8 nm which coarsened with proceeding crystallization up to ~10-12 nm. The supersaturation of bcc-Fe by Mo is witnessed by the presence of forbidden (100) line on electron diffraction patterns and by an increase of lattice parameter against the value for

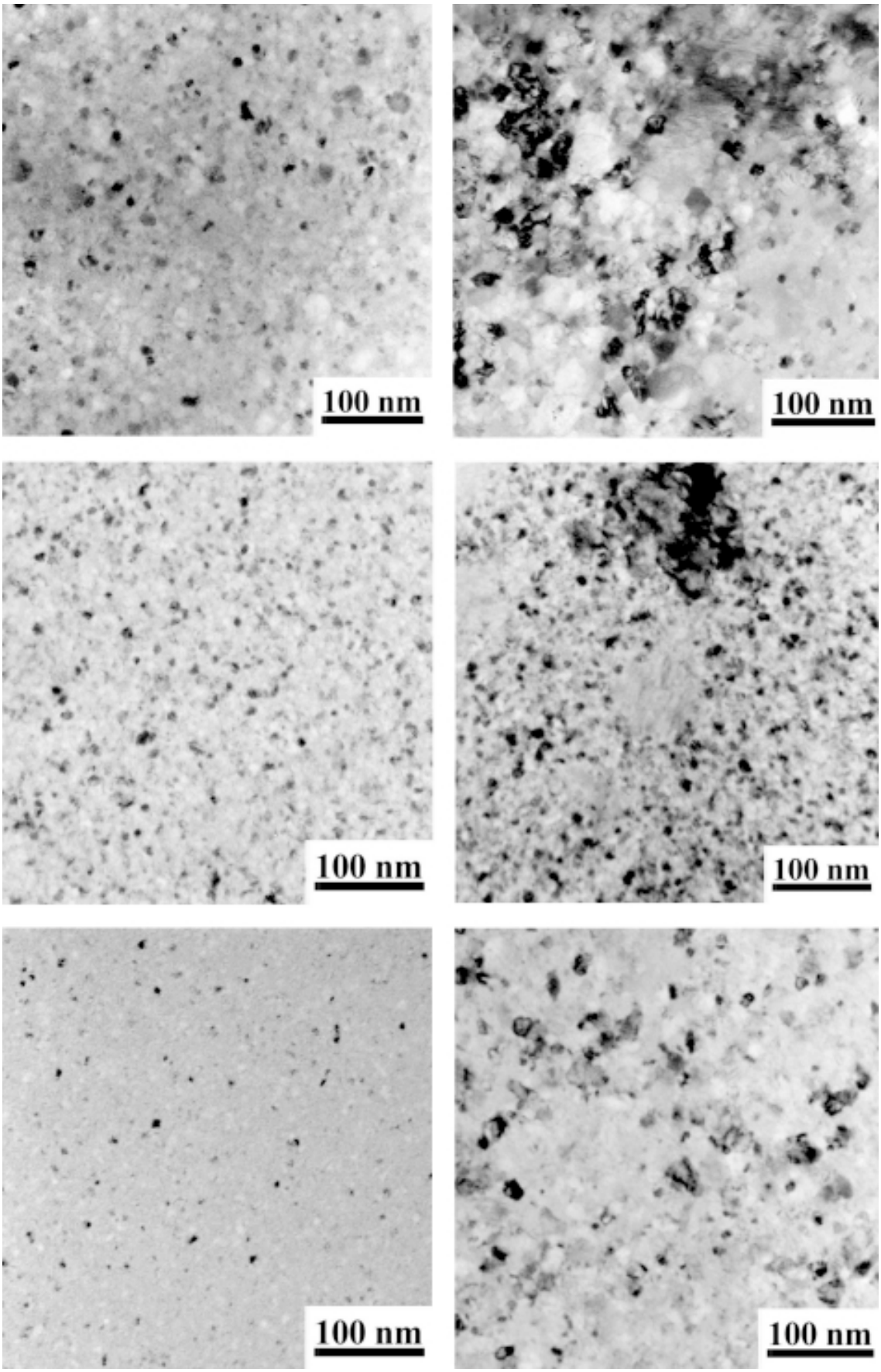

Fig. 3. Top: TEM images of $Fe_{80}Mo_8B_{12}$ after annealing at 800 (left) and 900K (right) for 30 min. Middle: TEM images of $Fe_{79}Mo_8Cu_1B_{12}$ annealed for 30 min at 750K (left) and at 930K (right). Bottom: TEM images of $Fe_{76}Mo_8Cu_1B_{15}$ annealed for 30 min at 800K (left) and at 930K (right).

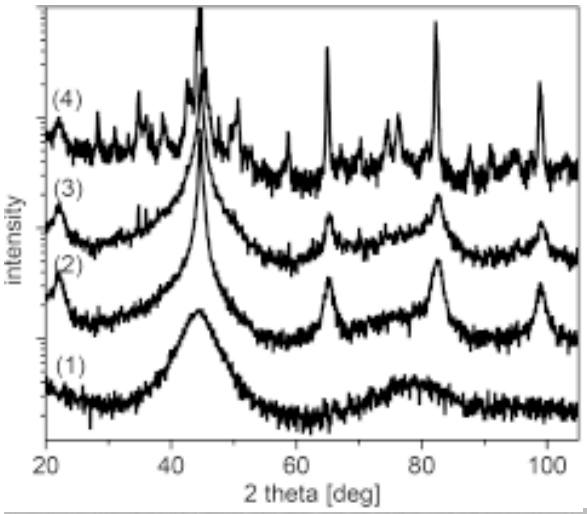

Fig. 4. X-ray patterns of $Fe_{79}Mo_8Cu_1B_{12}$ and $Fe_{76}Mo_8Cu_1B_{15}$ in as-quenched state and after annealing: curve (1) – as-quenched $Fe_{79}Mo_8Cu_1B_{12}$, curve (2) - $Fe_{79}Mo_8Cu_1B_{12}$ annealed at 750K for 30 min, curve (3) - $Fe_{76}Mo_8Cu_1B_{15}$ annealed at 800K for 30 min, curve (4) - $Fe_{79}Mo_8Cu_1B_{12}$ annealed at 973K for 30 min (after the second crystallization stage). Annealing at 973K leads to the same pattern for both compositions and is almost identical with the patterns for master alloy precursors.

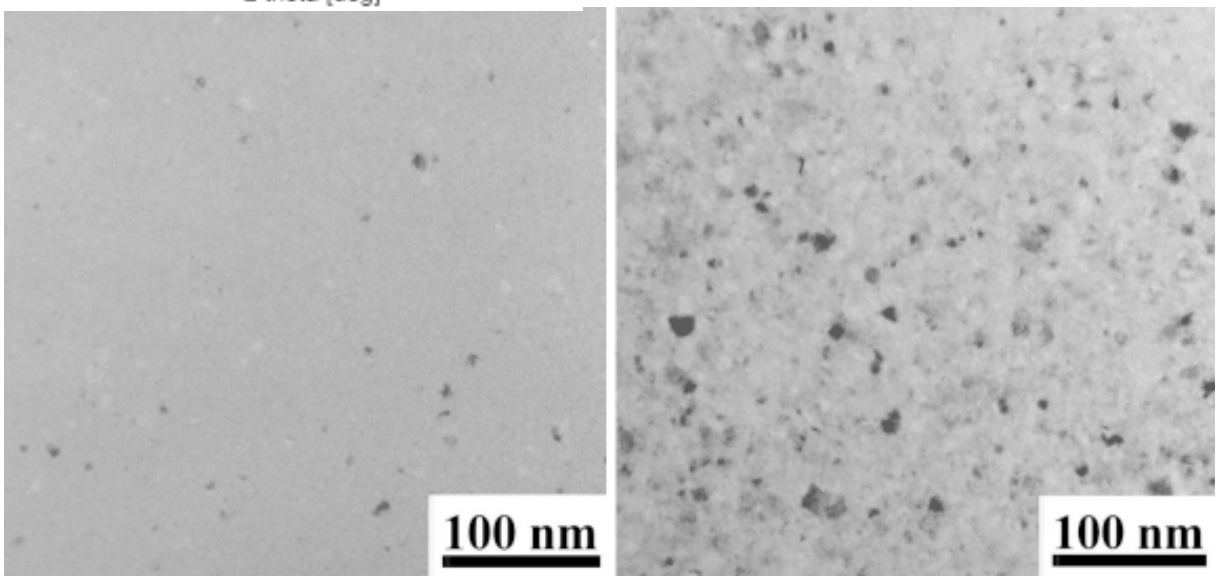

Fig. 5. The structure of $Fe_{74}Mo_8Cu_1B_{17}$ after annealing at 810 (left) and 930K (right) for 30 min.

pure bcc-Fe. The morphology, size and volume density of the grains is preserved even during the second transformation stage (above 900K), where additional larger globular grains of B_2Mo_2Fe are formed (Fig. 3, middle row). Similar situation is observed in $Fe_{76}Mo_8Cu_1B_{15}$ (Fig. 3, bottom row). However, the transformation begins at slightly higher temperature (~850K), the nanocrystalline grains exhibit lower supersaturation with Mo and attain the sizes of 5-8 nm only. Furthermore, the content of the nanocrystalline phase is significantly lower. The second stage (above 930K) again leads to formation of globular B_2Mo_2Fe and increase of the size of the bcc-grains (Fig. 4). A complete recrystallization, however, with only the change of morphology into polyhedric grains with lamellar structure [11], takes place above 973K. In both cases the final phases present after annealing to ~1000K are almost identical with those observed in the corresponding master alloys except for very low content of the Fe_3B phase in the ribbon samples.

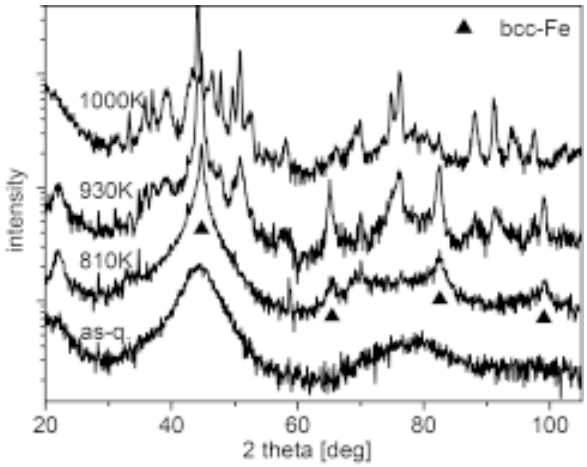

Fig. 6. X-ray patterns of $Fe_{74}Mo_8Cu_1B_{17}$ in as-quenched state and after annealing for 30 min. at 810 and 930K and $Fe_{71}Mo_8Cu_1B_{20}$ at 1000K/30 min (top curve). Solid upright triangles indicate the positions of the bcc-Fe reflections.

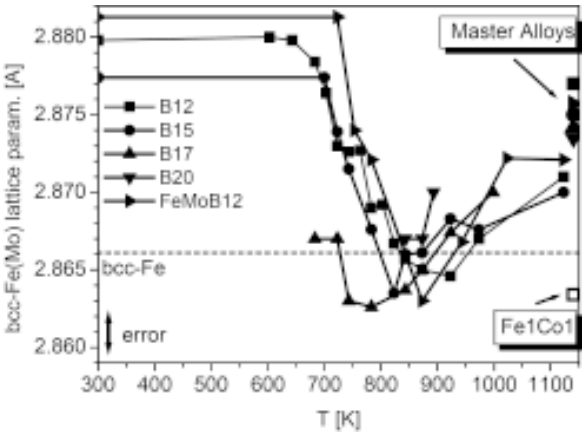

Fig. 7. Evolution of lattice parameter of bcc-Fe(Mo) phase in $Fe_{91-x}Mo_8Cu_1B_x$ system and in $Fe_{80}Mo_8B_{12}$ with thermal treatment; the values in as-quenched state were obtained from bottom (wheel) side of the samples. The numbers indicate boron content *x* (in at.%). The values for master alloys are shown on the right side of the graph, the symbol Fe1Co1 is for master alloy $(Fe_1Co_1)_{79}Mo_8Cu_1B_{12}$. The lines are to guide the eye only.

The transformation in as-quenched $Fe_{74}Mo_8Cu_1B_{17}$ and $Fe_{71}Mo_8Cu_1B_{20}$ ribbons begins by formation of more than one crystalline phase. In $Fe_{74}Mo_8Cu_1B_{17}$ small amounts of fine grains of bcc-Fe only slightly supersaturated with Mo are formed simultaneously with B_2Mo_2Fe in the first transformation stage, which is shifted to higher temperatures and exhibits a significantly smaller peak area on the DSC trace than for alloys with lower boron content, as shown in Fig. 1. The second stage is, on the other hand, more pronounced and shifted towards lower temperatures and leads to complete crystallization with formation of larger particles of both phases (Figs. 5 and 6). For $Fe_{71}Mo_8Cu_1B_{20}$ the two DSC peaks overlap each other and reflect the formation of mainly B_2Mo_2Fe and boride with $Fe_{23}B_6$ type of lattice. Only trace amounts of bcc-Fe phase were observed in the early stages of the reaction.

Lattice parameters of bcc-Fe(Mo) formed during crystallization process were determined from the positions of the first four Bragg peaks using the procedure described in [12] as well as by total pattern analysis using Bruker TOPAS software. Their values, shown in Fig. 7, are in accord with values from [10] and point to the increase of supersaturation of Fe with Mo with decreasing boron content and its evolution during the transformation process. It is interesting to note that the values for fully crystallized alloys with boron content not exceeding 15 at.% approach those observed in the precursor master alloys. These also exhibit a decrease with increasing content of B due to higher abundance of Mo-rich B_2Mo_2Fe phase. An even larger decrease of lattice parameter has been observed in (Fe-Co)-Mo-Cu-B system [7], however, due to formation of Co-Mo-rich phases. Detectable amounts of bcc-Fe phase are present only during intermediate stages of crystallization in $Fe_{71}Mo_8Cu_1B_{20}$ alloy.

3.2. Ribbon surfaces

According to XRD experiments, the as-quenched ribbons appear amorphous when analyzed from the air side, using the classical Bragg-Brentano configuration with point detector, and exhibit no presence of crystallinity in TEM after conventional sample preparation. However, X-ray patterns taken from the bottom (wheel) side of the ribbons (Fig. 8) reveal the presence of small maxima at the (110) and (220) angular positions of the bcc-Fe lattice.

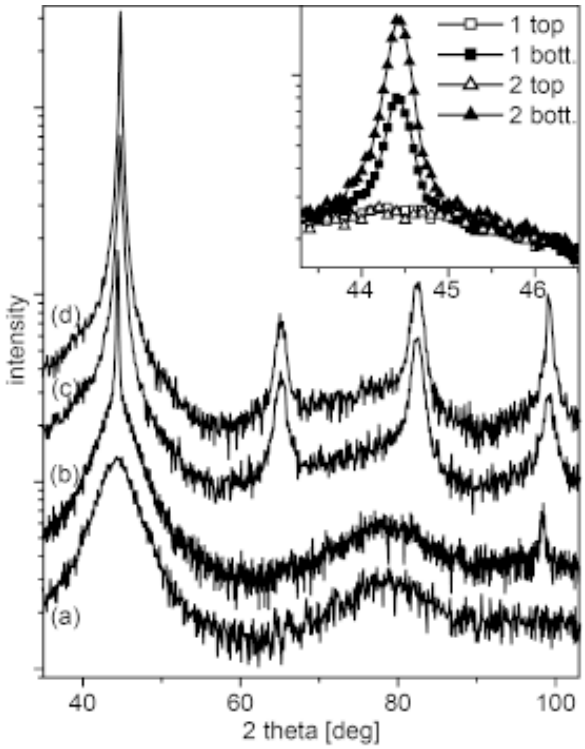

Fig. 8. A comparison of X-ray patterns from $Fe_{79}Mo_8Cu_1B_{12}$ taken from the top (curve a) and bottom (curve b) sides of the as-quenched 20-22 μm thick ribbon. The bottom side exhibits, besides amorphous halo, also small maxima at the positions of the (110) and (220) reflections of the bcc-Fe phase. The excess intensity of these maxima is present even after annealing up to 900K (curve c – top, curve d – bottom). Maxima at (200) and (211) positions exhibit no difference in intensities during the evolution of the bcc-phase with proceeding transformation. The inset shows details of the main (110) peak for curves (a) and (b) – pair of curves 1; curves 2 correspond to ribbons 16-18 μm thick.

This effect is most pronounced for the $Fe_{80}Mo_8B_{12}$ and $Fe_{79}Mo_8Cu_1B_{12}$ samples and decreases with increasing boron content, vanishing completely for $Fe_{74}Mo_8Cu_1B_{17}$ sample. In order to determine the influence of the quenching rate, ribbons with different thickness were prepared by varying the wheel speed as well as the casting temperature or the ejection pressure. Typical result from these experiments is shown in the inset of Fig. 8. Decrease of the ribbon thickness did not diminish the observed effect; thicker ribbons (above 25 mm) had the tendency to exhibit a certain amount of "normal" quenched-in bcc-Fe phase in addition to the observed (110) and (220) peaks. Similar results [2] were obtained on ribbons prepared from master alloys melt-treated at higher (1940K) and lower (1720K) temperatures as compared to the preselected value of 1830K for $Fe_{79}Mo_8Cu_1B_{12}$ which contained the lowest amount of crystallinity at the wheel side in the as-quenched state. The excess intensity of the (110) and (220) maxima remained present even after annealing up to 900K (Fig. 8, curves c, d) while the maxima at (200) and (211) positions exhibited no difference in intensities during the evolution of the bcc-phase with proceeding transformation.

The typical microstructure of the top, middle and bottom sides of the as-quenched ribbons with lower boron content (12 and 15 at.%) and for $Fe_{80}Mo_8B_{12}$ is shown in the left column of Fig. 9. Larger, ~300 nm sized particles are present in a layer at the bottom side, which, however, is not thicker than 1 mm; moving further into the "volume" of the ribbon these particles are replaced by much smaller, nanosized grains which quickly disappear completely, leaving only amorphous phase (Fig. 8, middle left). Both large and small particles exhibit only bcc-Fe reflections in the electron diffraction patterns; supersaturation with Mo is witnessed by the presence of (100) diffraction ring. The top ~0.5 mm thick layer contains small number of blob-like particles of B_2Mo_2Fe and bcc-Fe(Mo) embedded in amorphous matrix. The evolution of the microstructure with annealing is shown in the right column of Fig. 9. While the amorphous phase in both top and bottom layers transforms into nanocrystalline grains in the same manner as described in the previous section for the "volume" of the ribbons, no significant change of morphology or size is observed in the "as-quenched" particles during the first stage of transformation, in accord with the X-ray observations shown in Fig. 8.

Additional information about the surface structure was obtained from 2D X-ray patterns taken with the area detector (GADDS 32, Bruker, taken at HMI/BESSY synchrotron, Berlin). The frame taken from the bottom side of as-quenched ribbon shown in Fig. 10 (left) confirms the presence of small peak at the position of [110] reflection of bcc-Fe in addition to the amorphous halo. Scan from the top side shows the presence of small amount of randomly oriented B_2Mo_2Fe embedded in amorphous phase. No particular preferential orientation has been observed at the top side of the ribbon

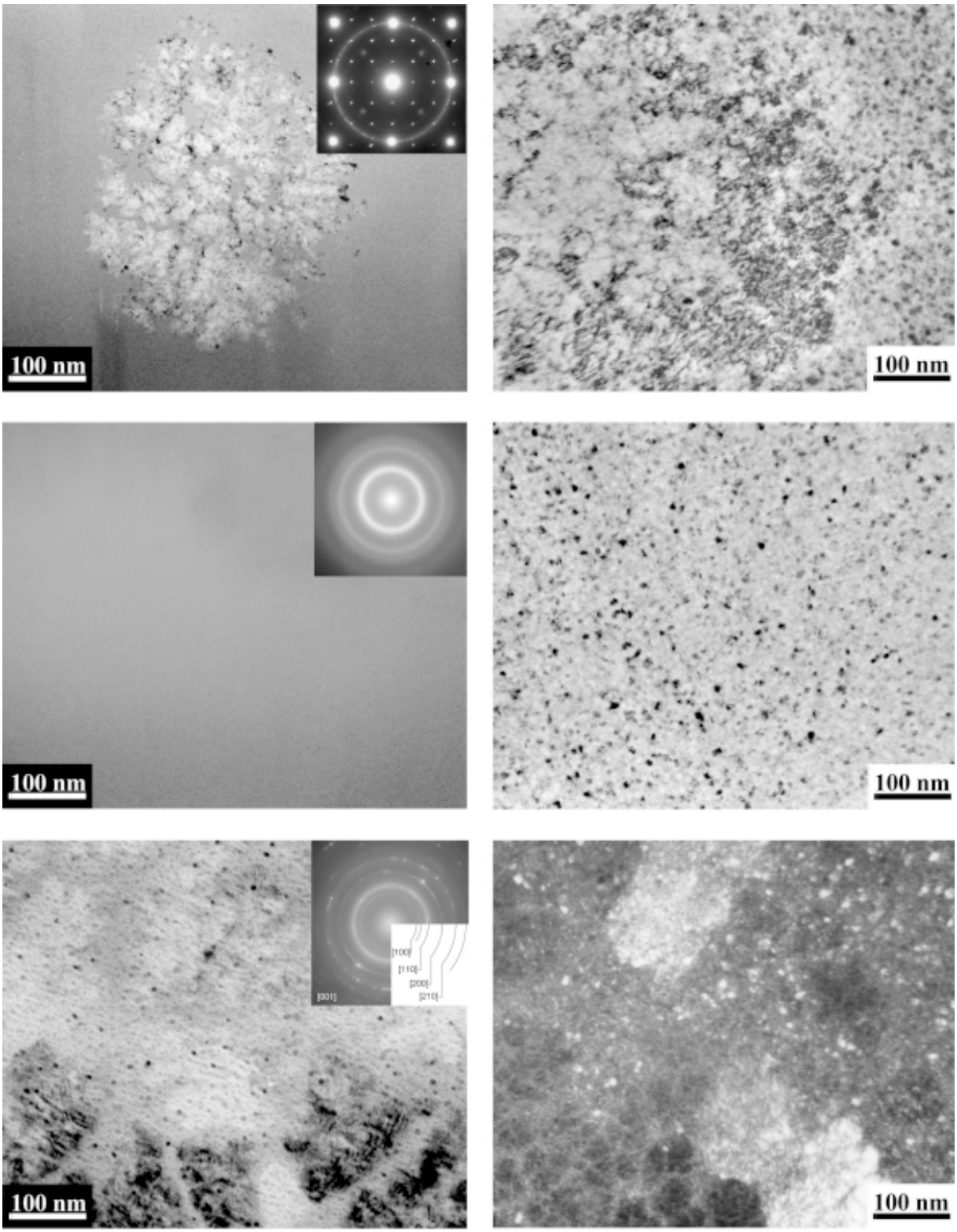

Fig. 9. CS TEM of $Fe_{79}Mo_8Cu_1B_{12}$ in as-quenched state (left) and annealed at 850K for 30 min (right) showing the microstructure at the air side (top), in the volume of the ribbon (middle) and at the wheel side (bottom). Selected area electron diffraction pattern (inset) from the bottom side shows, besides amorphous halo, the presence of bcc structure with forbidden reflections at (100) due to supersaturation of bcc-Fe with Mo. ED from the top side ([001] zone axis) shows, besides intense (110) reflections also weaker forbidden spots (100) of bcc-Fe(Mo) resulting from supersaturation and small intense spots of B_2Mo_2Fe present in blob-like particles in a layer close to the top surface. These particles exhibit no significant growth or morphology change throughout the entire transformation process.

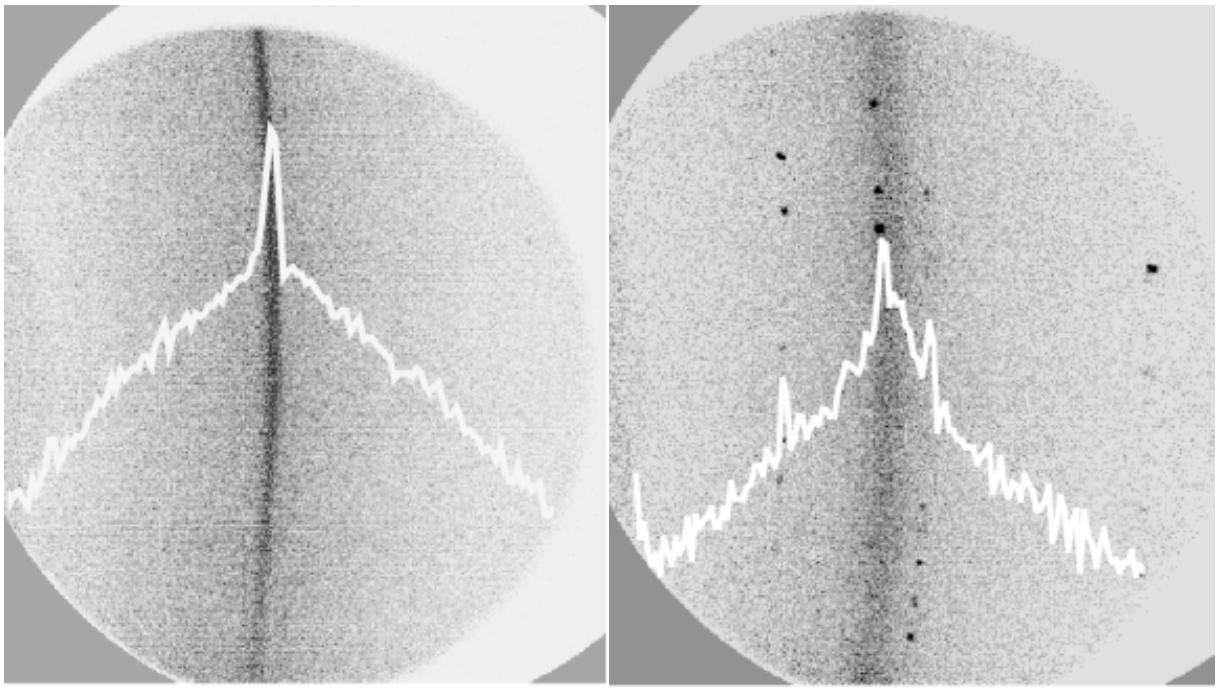

Fig. 10. 2D X-ray scans of as-quenched $Fe_{79}Mo_8Cu_1B_{12}$ taken from bottom (left) and top (right) sides, angular range two-theta 45.4 to 58.7 deg., radiation wavelength 0.176 nm. The insets are two-theta scans (in log scale) after integration, showing the presence of small amount of quenched-in bcc-Fe phase ([110] reflection) and small amount of B_2Mo_2Fe ([201], [220], and [211] reflections) above the amorphous halo on the bottom and top sides, respectively. The quantity of B_2Mo_2Fe is at the limit of detection by classical X-ray analysis with point/line detector.

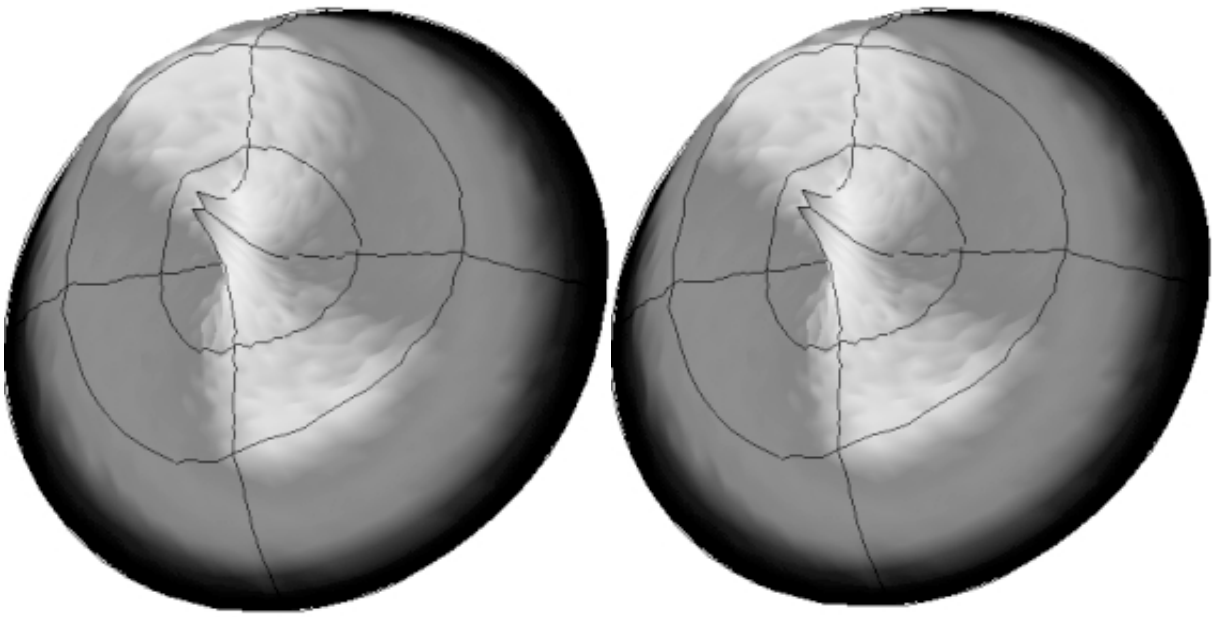

Fig. 11. The pole figure at [110] position of the bcc-Fe phase taken from bottom (left) and top (right) sides of as-quenched $Fe_{79}Mo_8Cu_1B_{12}$. Long ribbon axis horizontal with respect to the figures.

Table 1. Scheme of quenching rates $q = \partial T/\partial t$ and structure formed across the ribbon thickness for conventionally and anomalously behaving single-roll rapidly quenched ribbons. The implicit technologically-given variation of q across the ribbon from maximal (at the wheel side) to minimal (at the air side) is indicated in the leftmost column.

q_a = min	air side	conventional		anomalous	
	top	cryst.	cryst.	amorph.	amorph./cryst.
	middle	cryst.	amorph./cryst.	amorph.	amorph.
	bottom	cryst.	amorph.	amorph.	cryst.
q_a = max.	wheel side	q_1	$q_2 > q_1$	$q_3 > q_2$	q_a = ?

also on the pole figures in as as-quenched (Fig. 11, right) or annealed states. The bottom side (Fig. 11, bottom) exhibits a certain degree of preferential orientation of the quenched-in bcc-phase, mainly in the (110) direction; further details from the texture analysis will be presented elsewhere.

4. DISCUSSION

The investigated Fe-Mo-Cu-B system has been found to be, with the exception of the surface layers, easily amorphisable (as checked by X-ray and TEM) for thicknesses 16-25 microns, widths 3-12 mm (as tested), wheel speeds from 25 m/sec (the lowest value tested) to 40 m/sec and different casting temperatures. Neither increase or decrease of the effective quenching rate lead to improvements with respect to the surface effects; rather, optimal set of quenching rates provided minimal, yet existing, quenched-in crystallinity at the wheel side of the ribbons. The amount of quenched-in crystallinity at the bottom side did not exceed 5 vol.% as estimated by X-ray analysis. In all cases the air side of the ribbon was without detectable peaks of bcc-Fe phase and the volume of the ribbon was TEM-amorphous. The same effect was observed also in $Fe_{80}Mo_8B_{12}$, indicating that the presence of Cu has been of importance only for the overall nanocrystallization process, not for the amorphisation. The influence of the surface of the casting Cu-wheel was also experimentally assessed; different wheel surface treatments and their combinations were used prior to rapid quenching – machining, turning, polishing, cold-rolling, etc. No correlation of the observed effects with the wheel surface or ribbon surface roughness on either bottom or top sides of the ribbons could be observed [2,7]. Also no additional content of Cu was observed due to the contact of the ribbon with the wheel.

The content of quenched-in B_2Mo_2Fe on the air side was found to increase with increasing boron content and decreasing quenching rate as well as with decreasing casting temperature. It is to be noted, however, that this effect is confined to a very thin surface layer on the air side, beneath which the samples exhibit purely amorphous structure. The effect can be eliminated completely (or enhanced) for samples with boron content above 15 vol.% by slight adjustment of casting conditions.

The phases present in polycrystalline master alloy precursors were identified by X-ray analysis. In all cases - induction furnace and arc-melt $Fe_{80}Mo_8B_{12}$ and $Fe_{91-x}Mo_8Cu_1B_x$, x=12-20 - the main phase observed, besides bcc-Fe(Mo) with lattice parameters shown in Fig. 7, is the tetragonal B_2Mo_2Fe and tetragonal Fe_3B. The amount of Fe_3B increases only very slightly with increasing boron content; no observable changes in the content of B_2Mo_2Fe were observed.

In ribbon samples the formation of B_2Mo_2Fe depends on the mutual availability of Mo and B. Lower boron content and relatively high mutual solubility of Mo in Fe [10] lead to higher supersaturation of Fe with Mo, which decreases with proceeding nanocrystallization. Increased boron content results in preferential formation of B_2Mo_2Fe and lower initial supersaturation of bcc-Fe. An explanation of this effect can be found in the assumption that small locally ordered regions rich in Mo and B are preferentially formed (or preserved) upon rapid quenching. At sufficiently high boron content (17 and 20 at.%) these regions transform preferentially, leaving amorphous remains rich in Fe and B (with only slight traces of Mo) to form simultaneously the bcc phase and especially borides, as

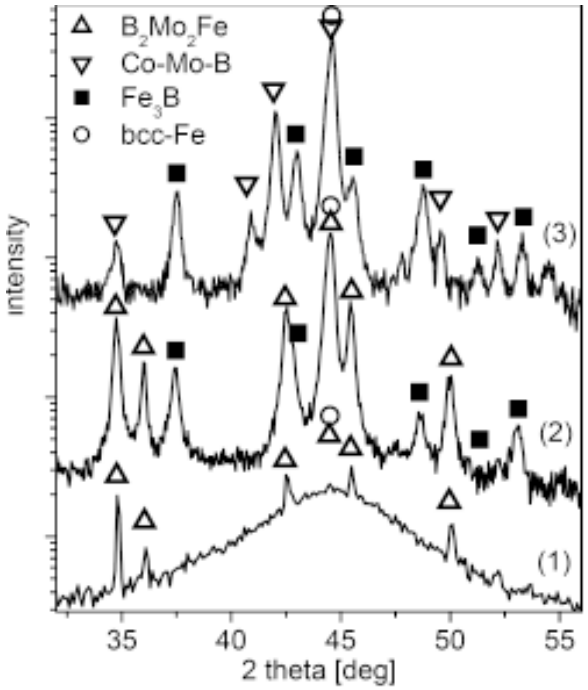

Fig. 12. X-ray patterns from master alloys $Fe_{79}Mo_8Cu_1B_{12}$ (curve 2) and $(Fe_3Co_1)_{79}Mo_8Cu_1B_{12}$ (curve 3) showing different phases present in dependence on Co content. Diffraction pattern from top side of as-quenched ribbon with higher boron content (curve 1, $Fe_{74}Mo_8Cu_1B_{17}$) shows the presence of small amounts of quenched-in B_2Mo_2Fe phase due to slightly lower temperature of the melt prior to casting.

observed. The evolution of lattice parameter of bcc-Fe(Mo) during nanocrystallization (especially in ribbons with lower content of B) may then be ascribed to the transformation of thermodynamically less stable regions poorer in B and containing the remaining portion of Mo without their significant chemical rearrangement. The growth ceases with exhaustion of these regions, which is in accord with the decreasing availability of these regions in dependence on B and also with their small size and amount. The decrease of lattice parameter with proceeding nanocrystallization may be attributed either to the diffusion of Mo towards the nanograin interface or to the progressive inclusion of regions containing still less Mo; further high-resolution elemental mapping experiments to clarify this issue are in progress.

Substitution of Fe by Co in the $(Fe_{1-x}Co_x)_{79}Mo_8Cu_1B_{12}$ for x=0 - 0.5 leads to a change in the type of phases contained in the master alloy (Fig. 12). For Co/Fe < 1/3 the situation is the same as for Fe-Mo-Cu-B alloys. For higher Co contents phases containing Co-Mo are formed, namely orthorhombic CoMoB (Pnma, no. 62) with parameters a=0.5741nm, b=0.3232nm, and c=0.6634nm, instead of B_2Mo_2Fe. Increased content of tetragonal Fe_3B is also observed. These Co-Mo phases, according to the phase diagrams, have somewhat lower melting temperature than Fe-Mo alloys and thus can be expected to form sufficiently homogeneous melt before its rapid quenching. Also, Mo is known to stabilize the fcc lattice structure of Co, thus facilitating amorphisation due to need of much more drastic atomic rearrangements necessary to create the bcc-lattice which is the first crystalline “equilibrium” phase formed during (possibly insufficiently) rapid quenching or upon crystallization from amorphous state, in accord with the texture observed in [7]. Fully amorphous ribbons were obtained by rapid quenching in this system for Co/Fe ≥ 1/3 while lower Co content has lead to the same surface effects as observed above for the $Fe_{91-x}Mo_8Cu_1B_x$ system with $x \leq 15$.

With respect to the results from different quenching experiments described above, there remains open question if there exists a minimum (i. e. optimal) quenching rate to produce fully amorphous state. Alternatively, the question is about the existence of a set of such parameters, especially quenching conditions and above all the optimal melt structure prior to quenching. The generally accepted scheme [13] relating TTT diagram and critical cooling rate for glass formation (bypassing the nose of the TTT curve during quenching) is schematically depicted in Table 1. While insufficient overall quenching rate (q_1) leads to polycrystalline structure, increase of q ($q_2 > q_1$) enhances amorphisation from the bottom side where the local q_a is implicitly highest; sufficiently high $q_3 > q_2$ leads to fully amorphous structure. As shown above, the Fe-Mo-Cu-B system does not behave according to this pattern; the apparent q seems to change over the ribbon thickness in an unexpected way.

It has been shown that local atomic ordering in amorphous Fe-B type alloys is of bcc type [14]. One of the best close-packed local arrangements of constituent atoms in Fe-B may be tetrahedral. Similar arrangements, slightly distorted and deformed, respecting the complexity of the alloy melt and its tendencies to retain local chemical order-

ing or even to form icosahedral-like ordering, depending on the temperature region of the melt, can be expected to be present above liquidus and after quenching. The observed bcc local ordering in amorphous and subsequent immediate crystalline state can be achieved relatively easily by slight rearrangement over short distances, with Mo and/or B being easily accommodated in the lattice in the form of supersaturated solid solution. A combination of B-Mo or Co-Mo leads to phases with local ordering different from bcc – rhombohedral, tetragonal, hexagonal, *etc.*, which requires higher degree of local atomic rearrangement to form the bcc structure either in the undercooled melt or during crystallization. Cluster structure in the melt different from local ordering of the amorphous or primary crystalline phase then implies a need for a specific "relaxation" time to perform the rearrangement, enhancing glass-forming ability and/or stabilizing the amorphous phase. Too high quenching rate, typical for the bottom layer of the ribbon then may reflect the bcc-like structure of the melt (with time in the undercooled liquid state insufficient for rearrangement), while lower quenching rates in the layers above, having already somewhat lower temperature of the melt, may preserve a local structure corresponding to this melt temperature region and being unlike bcc, promoting easy amorphisation. This effect may imply formation of a general phase field during quenching [15] accompanied by a (slight) compositional gradient or solute drag across the ribbon thickness during solidification; it is to be noted, however, that no observable compositional gradient has been found across the ribbon thickness, as described in the experimental section above.

It is worthwhile to note that the morphology seen in CS TEM from the bottom side (Fig. 9) is very similar to fractal-like precipitates observed during crystallization of amorphous Si or Ge layers deposited on Al [16]. The investigation of formal similarity between the two processes, correlation with the observed bottom layer texture and possible phase field effects to clarify the micromechanisms controlling the observed phenomena is under progress.

While attractive for physical research, Fe-Mo-Cu-B ribbons with three types of layers prepared by a single operation might prove potentially of technical interest. Mechanically hard, wear resistant top layer, soft magnetic Fe(Mo)-containing bottom layer and the middle (paramagnetic or ferromagnetic) amorphous carrier layer with high strength and good ductility represents a type of functionally graded material for diverse applications. Besides, the overall magnetic properties of the ribbon indicate its attractiveness as possible material with magnetocaloric effect tunable by compositional tailoring [4].

5. CONCLUSIONS

The results from standard investigations of the formation of amorphous state and its transformations were presented for the nanocrystal-forming $Fe_{91-x}Mo_8Cu_1B_x$ (x=12-20) system. The importance of addition of Cu as nanocrystal former was shown on the case of $Fe_{80}Mo_8B_{12}$. Compositional dependence of crystallization temperatures and crystallization mechanism were analysed. It was shown that a change of mechanism from a two-stage (primary-like) process to a single stage (polymorphous-like) transformation takes place with increasing boron content; boride phases are formed alongside or instead of bcc-Fe(Mo) for alloys with 17 and 20 at.% of boron, respectively. The crystallization products were identified as bcc-Fe(Mo) with the degree of supersaturation decreasing with increasing boron content, B_2Mo_2Fe, $Fe_{23}B_6$ and small amounts of Fe_3B. The phases formed in the crystallization process correspond well to those observed in the polycrystalline master alloy precursors.

Special effects related to the appearance of crystalline phases at the surface layers of as-quenched ribbons were investigated which contradict the usual pattern of surface crystallinity formation due to insufficient quenching rates or glass forming ability. Kinetic and structure analyses have shown negligible effect of surface-induced crystal nucleation and growth initiated at the quenched-in crystal sites on the volume crystallization. Disappearance of the surface effects was correlated with changes of alloy composition and with addition of another element. The existence of optimal quenching conditions, solute drag or concentration profile was discussed with respect to the possible micromechanisms responsible for the observed phenomena. The hypothesis about their possible correlation with quenching-in of melt structure and local ordering during during solidification was suggested. Potential technical application of the systems as functionally graded or magnetocaloric materials was commented.

ACKNOWLEDGEMENT

This work was supported by the grants VEGA 2/0157/08, 1/4011/07, APVT-51-052702, 99-017904,

20-008404, 0413-06, MSM6198959218 and COST P17 (APVV-COST-031-06) and by the SAS Center of Excellence "Nanosmart". Thanks are due to E. Illekova for DSC measurements, to I. Zizak and G. Schumacher (HMI/BESSY, Berlin) for help with synchrotron radiation measurements and to Dr. O. Heczko (HUT, Helsinki) for texture analysis.

REFERENCES

[1] E. Illeková, D. Janičkovič, M. Miglierini, I. Škorvánek and P. Švec // *J. Magn. Magn. Mater.* **304** (2006) e636.
[2] D. M. Kepaptsoglou, M. Paluga, M. Deanko, D. Müller, C. F. Conde, E. Hristoforou, D. Janičkovič and P. Švec // *Journal of Microscopy* **223** (2006) 288.
[3] C. F. Conde, A. Conde, D. Janickovic and P. Švec // *Journal of Magn. Mag. Mater.* **304** (2006) e739.
[4] V. Franco, C. F. Conde, J.S. Blázquez, A. Conde, P. Švec, D. Janičkovič and L. F. Kiss // *J. App. Phys.* **101** (2008) 093903 1.
[5] G. Vlasak, C. F. Conde, D. Janičkovič and P. Švec // *J. Magn. Magn. Mater.* **304** (2006) e580.
[6] S. Akiyama, S. Nakagawa and M. Naoe // *IEE Trans. on Magnetics* **27** (1991) 5094.
[7] M. Paluga, P. Mrafko, P. Švec, D. Janičkovič, E. Illeková and C. F. Conde // *Advances in Electrical and Electronic Engineering* **4** (2005) 63.
[8] C. F. Conde and A. Conde // this volume.
[9] V. Raghavan // *Journal of Phase Equilibria* **24** (2003) 449.
[10] H. Okamoto, *Phase diagrams of binary iron alloys* (ASM International, Materials Park, 1993), p. 214.
[11] E. Illeková, P. Švec and M. Miglierini // *J. Non-Cryst. Sol.* **353** (2007) 1970.
[12] B. D. Cullity and S. R. Stock, *Elements of X-ray Diffraction, 3rd Edition* (Prentice Hall, Upper Saddle River, 2001).
[13] H. A. Davies // *Phys. Chem. Glasses* **17** (1976) 337.
[14] Y. Hirotsu, T. Ohkubo and M. Matsushita // *Microsc. Res. Tech.* **40** (1998) 284.
[15] D. Danilov and B. Nestler // *Discrete Cont. Dyn. Systems* **15** (2006) 1035.
[16] G. Raghavan and R. Rajaraman // *Phys. Rev. B* **68** (2003) 012104.